Annals of Nuclear Medicine (2022) 36:420–426
https://doi.org/10.1007/s12149-022-01721-z

SHORT COMMUNICATION

Initial evaluation of a new maximum-likelihood attenuation correction factor-based attenuation correction for time-of-flight brain PET

Tetsuro Mizuta[1] · Tetsuya Kobayashi[2] · Yoshiyuki Yamakawa[1] · Kohei Hanaoka[3] · Shota Watanabe[3] · Daisuke Morimoto-Ishikawa[3] · Takahiro Yamada[3] · Hayato Kaida[3,4] · Kazunari Ishii[3,4]

Received: 16 September 2021 / Accepted: 17 January 2022 / Published online: 9 February 2022

Abstract

Aim The aim of this study was to evaluate an image reconstruction algorithm, including a new maximum-likelihood attenuation correction factor (ML-ACF) for time of flight (TOF) brain positron emission tomography (PET).

Methods The implemented algorithm combines an ML-ACF method that simultaneously estimates both the emission image and attenuation sinogram from TOF emission data, and a scaling method based on anatomical features. To evaluate the algorithm's quantitative accuracy, three-dimensional brain phantom images were acquired and soft-tissue attenuation coefficients and emission values were analyzed.

Results The heterogeneous distributions of attenuation coefficients in soft tissue, skull, and nasal cavity were sufficiently visualized. The attenuation coefficient of soft tissue remained within 5% of theoretical value. Attenuation-corrected emission showed no lateral differences, and significant differences among soft tissue were within the error range.

Conclusion The ML-ACF-based attenuation correction implemented for TOF brain PET worked well and obtained practical levels of accuracy.

Keywords Attenuation correction · ML-ACF · TOF brain PET

Introduction

Attenuation correction is an important requirement for quantitative positron emission tomography (PET). Computed tomography-based attenuation correction (CT-AC), which uses the CT images obtained for diagnostic purposes for attenuation correction, has been the subject of numerous studies. However, because the PET and CT scans are performed sequentially, the images are not perfectly aligned because of respiratory and/or patient motion, and attenuation correction artifacts due to spatial mismatches are unavoidable [1, 2]. With consideration of reducing radiation exposure, the PET-CT guidelines for the diagnosis of dementia state that low-dose CT and optimization of positioning are necessary to minimize exposure to the eye lens, with most patients also having existing MRI images for morphologic diagnosis [3]. Furthermore, the initial and running costs can be reduced if CT-AC is unnecessary. For these reasons, we consider it necessary to develop an attenuation correction for brain PET scans that does not require CT. The join-estimation method to obtain attenuation factor only from emission data has been proposed since the early state of non-time-of-flight (TOF) PET [4]. This method resulted in insufficient accuracy due to contamination between emission and attenuation and could not implemented in practical use. Recently some researchers showed that TOF PET data allowed stable estimation of scaled (non-quantitative) attenuation factor [1, 2, 5]. Furthermore, some scaling methods which can quantify the attenuation factor were proposed and validated [6, 7]. In this study, we

✉ Tetsuro Mizuta
mizuta@shimadzu.co.jp

1 Medical Systems Division, Shimadzu Corporation, 1, Nishinokyo Kuwabara-cho, Nakagyo-ku, Kyoto 604-8511, Japan

2 Technology Research Laboratory, Shimadzu Corporation, Kyoto, Japan

3 Division of Positron Emission Tomography, Institute of Advanced Clinical Medicine, Kindai University, Osakasayama, Japan

4 Department of Radiology, Kindai University Faculty of Medicine, Osakasayama, Japan

implemented the maximum-likelihood attenuation correction factor (ML-ACF) method [2] combined with the scaling method [6] which was modified to coincide the mode of the intensity histogram of attenuation image with 0.096 cm^{-1} for TOF brain PET scanning. Quantitative evaluation of the algorithm was performed using phantom experiments.

Materials and methods

Scanner configuration

The TOF PET scanner used (SET-5002, Shimadzu Corporation, Kyoto, Japan) had a sufficient axial field of view (FOV) of 162 mm to allow whole brain scanning (Fig. 1). The scanner consists of three detector rings of 300 mm diameter, with each ring consisting of 16 detector modules. Each detector module is in coincidence with the opposing fifteen modules to provide an effective transaxial FOV of more than 268 mm. Each detector module consists of a single layer of lutetium—including crystals, optically coupled to a silicon photomultiplier (Multi-Pixel Photon Counter, S14161-3050HS-04, Hamamatsu Photonics, Hamamatsu, Japan). The small crystal elements with its size of 2.1 (X) × 2.1 (Y) × 15 mm (depth) are arranged in a 24 (X) × 24 (Y) array. During data acquisition, both prompt and delayed events are saved in list-mode format, and a three-dimensional (3D) image is reconstructed at an isotropic voxel size of 1.1 mm with a matrix of 240 (X) × 240 (Y) × 148 (Z). As typical physical performance, we obtained the spatial resolution FWHM at the center of FOV as 2.5 mm (radial), and the hot contrast ⊿QH (10 mm) in the image quality evaluation as 49.9% according to NEMA NU2-2012. However, the image quality was evaluated using a cylindrical phantom with an inner diameter of 200 mm instead of a IEC Body Phantom for background region by considering of the transaxial FOV.

Image reconstruction flow

We implemented the following image reconstruction flow [6] consisting of nine processing steps including ML-ACF (Fig. 2).

[Step1] Reconstruct the non-attenuation corrected (NAC) image with the ordered-subset expectation–maximization (OS-EM) algorithm [8].

[Step 2] Generate the uniform attenuation map μ_U using intensity-based thresholding of the NAC image, and combine it with the pre-defined headrest attenuation map μ_{HR} based on the actual structure to create the initial attenuation map $\mu^{(0)} = \mu_U + \mu_{HR}$.

[Step 3] Calculate the TOF scatter + random sinogram, referred to as *bias* sinogram in this paper, b by subtracting the attenuated TOF forward projection of the attenuation- and scatter-corrected non-TOF emission image λ_{NT} from the TOF prompt sinogram p as follows:

$$b_{it} = p_{it} - a_i^{(0)} \sum_j c_{ijt} \lambda_{NT,j}.$$

Here, b_{it} and p_{it} present the bias and the prompt count at tth TOF bin at ith LOR, respectively, and c_{ijt} is the geometric sensitivity of that photons emitted from jth voxel is detected at tth TOF bin of ith LOR. In the reconstruction ofλ_{NT}, the random correction is applied by subtracting the delayed event sinogram from the non-TOF prompt sinogram, and the scatter correction is applied by adding estimated scatter sinogram to estimated true sinogram in the non-TOF OSEM reconstruction. Here, the scatter sinogram was estimated iteratively by alternating the non-TOF OSEM reconstruction and the non-TOF single scatter simulation [9] using $\mu^{(0)}$ with tail-fitting. Attenuation correction is also applied using $\mu^{(0)}$.

[Step 4] Estimate the mask sinogram by intensity-thresholding of the forward projection sinogram of μ_U.

[Step 5] Using initial attenuation factor sinogram $a^{(0)}$, calculate the non-quantitative activity image λ and the

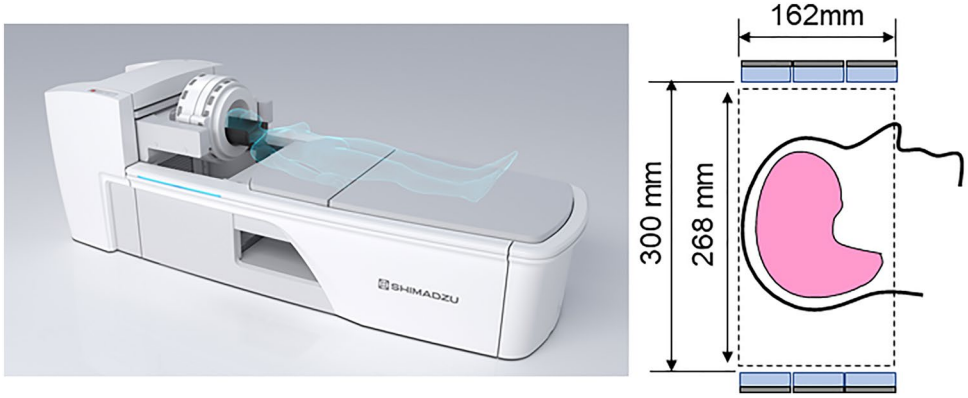

Fig. 1 Photograph and schematic configuration of the TOF PET scanner SET-5002

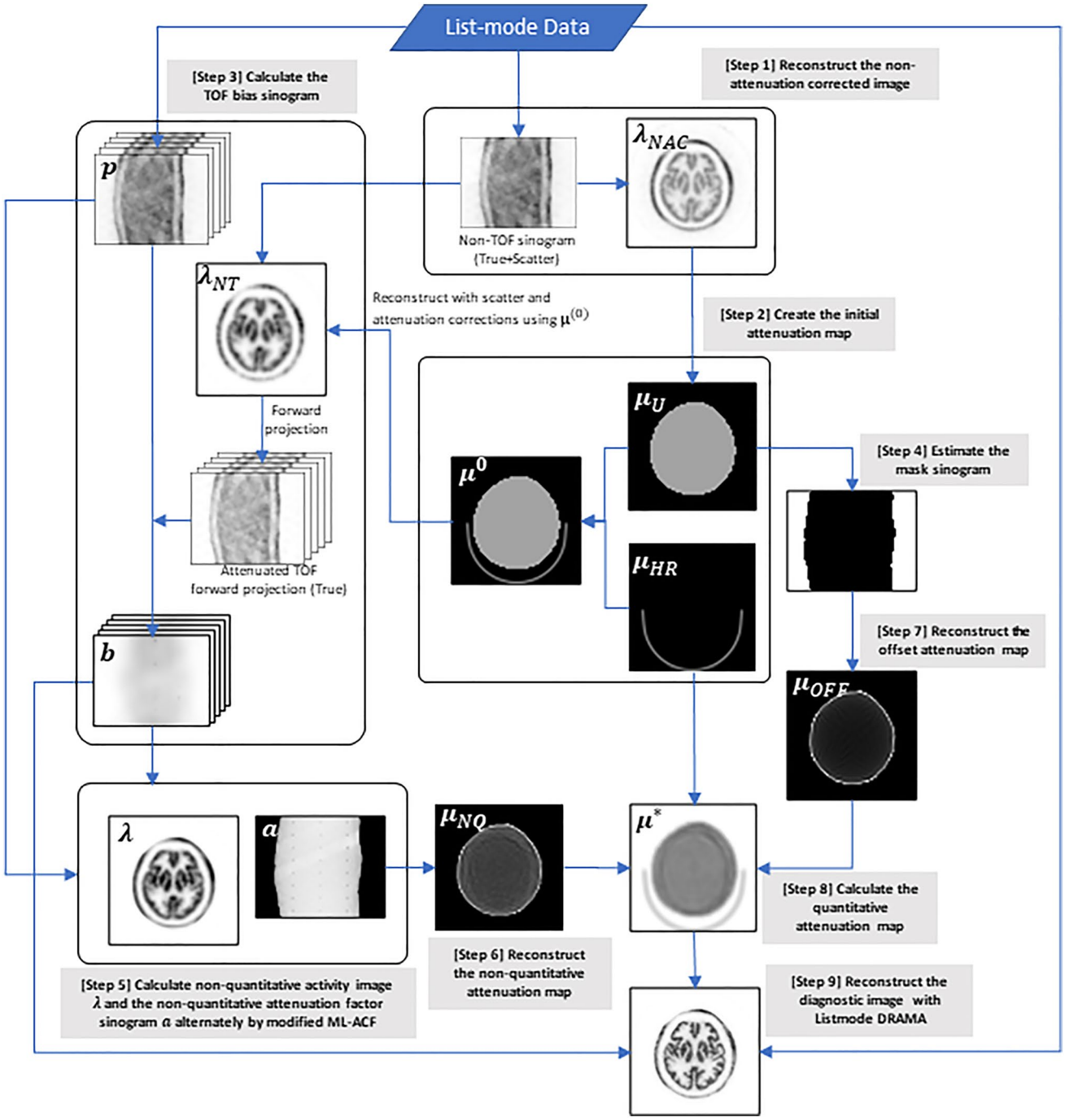

Fig. 2 Image reconstruction flow diagram for the transmission-less attenuation map generation method

non-quantitative attenuation factor sinogram a alternately by the ML-ACF [2] with small modifications as follows:

$$a_i^{(0)} = e^{-\sum_j \mu_j^{(0)} l_{ij}}$$

$$a_{\mathrm{HR},i} = e^{-\sum_j \mu_{\mathrm{HR},j} l_{ij}}$$

$$a_i^{(k+1)} = a_i^{(k)} \sum_t \frac{y_{it}^{(k)}}{y_i^{(k)}} \frac{p_{it}}{a_{\mathrm{HR},i} a_i^{(k)} y_{it}^{(k)} + b_{it}}$$

$$\lambda_j^{(k+1)} = \frac{\lambda_j^{(k)}}{\sum_{i,t} c_{ijt}} \sum_{i,t} c_{ijt} \frac{p_{it}}{a_{\mathrm{HR},i} a_i^{(k+1)} y_{it}^{(k)} + b_{it}},$$

where l_{ij} is the effective intersection length of ith LOR with jth voxel, and $y_{it}^{(k)}$ and $y_i^{(k)}$ are the non-attenuated TOF and non-TOF forward projection of activity image $\lambda^{(k)}$ of tth TOF bin of ith LOR:

$$y_{it}^{(k)} = \sum_j c_{ijt}\lambda_j^{(k)}$$

$$y_i^{(k)} = \sum_t y_{it}^{(k)}.$$

[Step 6] Reconstruct the non-quantitative attenuation map μ_{NQ} from the non-quantitative attenuation factor sinogram estimated at [Step 5] by OS-EM.

[Step 7] Reconstruct the offset attenuation map μ_{OFF} from the mask sinogram by OS-EM.

[Step 8] Calculate the quantitative attenuation map μ^* by

$$\mu^* = \mu_{\mathrm{NQ}} + \mu_{\mathrm{HR}} + \alpha\mu_{\mathrm{OFF}},$$

where the scaling factor α is determined to coincide the mode of the intensity histogram of μ^* with 0.096 cm^{-1}. Here, we assumed that human head almost consists of soft tissue.

[Step 9] Reconstruct the diagnostic image using the list-mode dynamic row-action maximum-likelihood algorithm (DRAMA) [10] with image-space point spread function modeling.

In this study, we combined the ML-ACF method with a scaling method (Step 8) that uses the predictive information that the linear attenuation coefficient (which accounts for most of the target area) is equivalent to water, thus enabling the clinical use of ML-ACF.

Experiments

To evaluate the accuracy of the attenuation correction applied to brain PET scans, we performed a phantom experiment using a 3D brain phantom [11] consisting of three non-uniform cold regions of skull, soft tissue (white matter), and nasal cavity, and a uniform hot region (gray matter). In the joint reconstruction algorithms of activity and attenuation including ML-ACF, the attenuation factors of the line of response (LOR) that does not pass through the hot region cannot be theoretically determined. To estimate all the attenuation factors, the object must be covered by the hot region. In clinical brain PET scans, the radioactive tracer is distributed over the whole head including the scalp, and the scalp plays the role of the hot region. However, this condition is not satisfied in the general phantom experiment. Therefore, in our experiments, the phantom was wrapped in a radioactive polymer sheet prepared by spraying a radioactive solution with an equal concentration to that of gray matter onto the sheet. The radioactivity concentration in the gray matter and pseudo-scalp was 38.8 kBq/ml (total dose at gray matter: 21.6 MBq) at scan start time, and emission data were acquired for 10 min.

Diagnostic images were reconstructed with and without attenuation correction with the list-mode DRAMA condition of subset 200, beta 200, and iteration 1, followed by a 3 × 3 × 3 median filter as a post filter. The voxel size was 1.1 mm isotropic. The non-attenuation-corrected image, uniform attenuation map, and quantitative attenuation map generated by the intermediate processing were extracted.

Analysis

To validate the accuracy of the quantitative attenuation map obtained in step 8, a histogram of linear attenuation coefficients within the phantom was calculated.

To estimate the quantitative error in the clinical analysis of brain PET, region of interest (ROI) analysis was performed on the diagnostic image obtained in step 9. Twenty small ROIs of 3 mm in diameter were placed in each of the left and right hot regions of seven areas: frontal, occipital, temporal, parietal, thalamus, striatum, and cerebellum.

Statistical analysis

For the left and right regions of the seven areas (all 14 ROI groups), the data are expressed as the mean ± SD. One-way ANOVA tests with post hoc Tukey–Kramer tests were used to compare all 14 individual areas and the seven sets of combined left and right areas. P values of < 0.05 were considered significant. All statistical analyses were performed with EZR (Saitama Medical Center, Jichi Medical University, Saitama, Japan).

Results

Figure 3 shows a non-attenuation-corrected image (A), a quantitative attenuation map (B), three diagnostic images of representative cross sections including the cerebellum, thalamus, and parietal lobe (C), and a histogram of linear attenuation coefficients calculated in increments of 0.005 cm^{-1} for the intra-subject area of the quantitative attenuation image (D).

The quantitative attenuation map (B) visually confirmed the heterogeneous distribution of attenuation coefficients in soft tissue, skull, and nasal cavity. In all sections, the histogram peak of the soft tissue was confirmed to be around 0.1 cm^{-1}, and the deviation from the theoretical attenuation coefficient value of water (0.096 cm^{-1}) was less than 5%.

Figure 4 shows diagnostic images and profile curves with and without attenuation correction by the present method. In the image without attenuation correction (A), the pixel values were underestimated because of the influence of

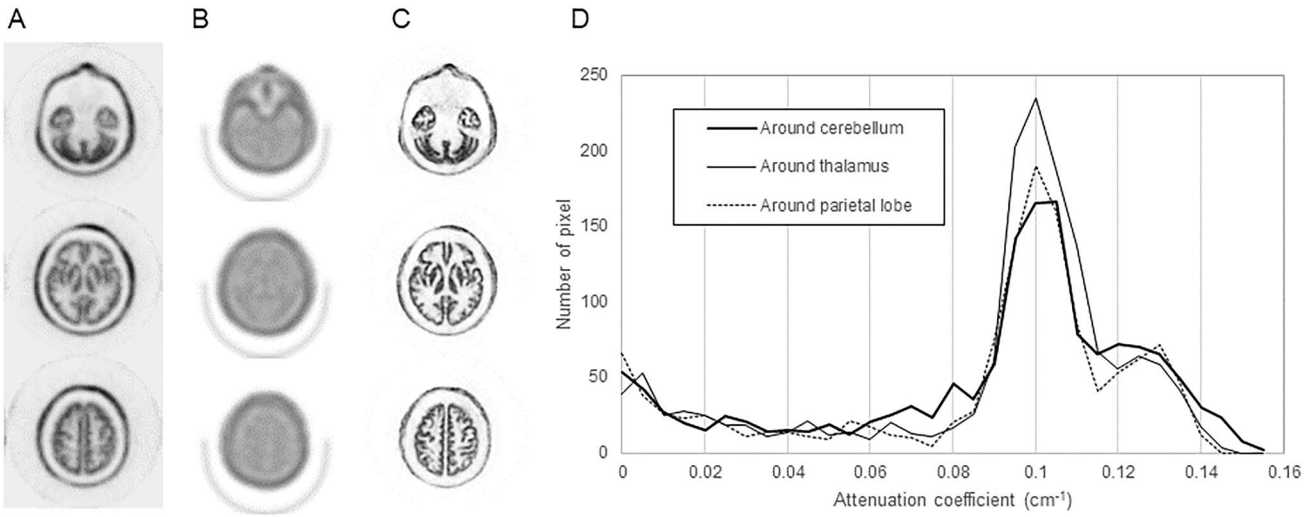

Fig. 3 Representative cross sections of a non-attenuation corrected image (**A**), quantitative attenuation map (**B**), diagnostic images (**C**), and histogram of the linear attenuation coefficient (**D**). These images (**A**–**C**) correspond from the top to around the cerebellum, thalamus, and parietal lobe

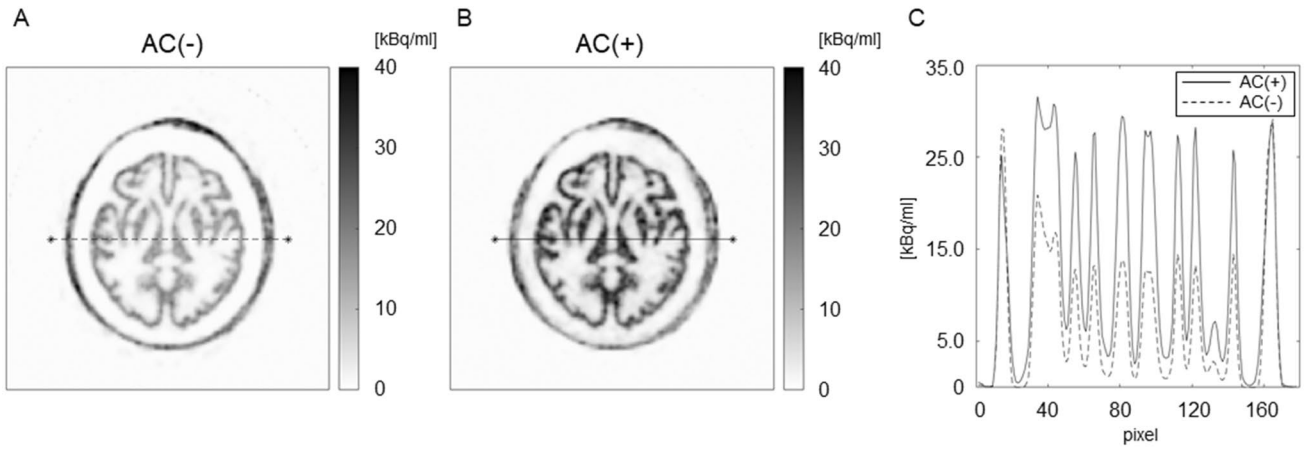

Fig. 4 Diagnostic images without attenuation correction (**A**), after attenuation correction (**B**), and profile curves (**C**)

attenuation as the depth through the subject increased, whereas with attenuation correction (B) the underestimation was removed. The profile curve (C) presented that the emission values were almost constant irrespective of the depth from the phantom surface.

Table 1 shows the maximum and average ROI values and their standard deviation errors of 20 ROIs placed on the left and right sides of all seven regions of the diagnostic image. Table 2 shows the results of statistical analysis.

For each of the seven regions of the diagnostic image, the difference in the average value between the left and right sides was within the standard deviation error, and no significant lateral difference was observed. However, the ANOVA test on the 14 ROIs showed the average values were underestimated by up to 34% (Occipital lobe R) compared with the theoretical activity concentration of 38.8 kBq/ml. In terms of the measured specific uptake value comparison between the seven hot region groups, significant differences were found between the cerebellum and all groups, and in some combinations of the other groups.

Discussion

In this study, we implemented a transmission-less attenuation correction method based on the ML-ACF method with the intention of applying it in clinical use, and performed an initial evaluation using a 3D brain phantom.

The results shown in Fig. 3A–C present that the attenuation correction was effective at compensating for the heterogeneity of the brain, such as that found across soft

tissue, skull, and nasal cavity. Visually, these attenuation maps were similar to conventional attenuation maps obtained at an external source and were considered sufficient for use as attenuation correction for PET. Figure 3D presents the quantitative validity of the attenuation coefficient, because the attenuation coefficient of soft tissue, which occupies most of the brain tissue and affects most of the attenuation correction, is very close to the theoretical value. The recovery of the count near the center of the subject in Fig. 4 indicates that the attenuation was properly corrected, because the profile curve shows a nearly constant concentration of activity irrespective of the depth from the subject surface.

Table 1 Results of the ROI analysis of seven regions

	Averaged measured value ($n=20$)	
	Max ± SD (kBq/ml)	Average ± SD (kBq/ml)
Frontal lobe		
R	35.9 ± 3.1	32.4 ± 2.5
L	35.3 ± 2.3	32.4 ± 2.4
Occipital lobe		
R	27.8 ± 3.8	25.4 ± 3.6
L	28.0 ± 3.8	25.7 ± 2.9
Parietal lobe		
R	31.1 ± 3.3	28.2 ± 2.7
L	30.3 ± 2.9	27.7 ± 2.9
Temporal lobe		
R	30.6 ± 2.7	28.2 ± 2.2
L	31.1 ± 2.4	28.7 ± 1.8
Thalamus		
R	32.9 ± 1.9	31.0 ± 1.7
L	32.1 ± 2.2	30.0 ± 1.8
Striatum		
R	34.8 ± 2.3	31.7 ± 1.5
L	34.0 ± 2.6	31.7 ± 1.9
Cerebellum		
R	39.0 ± 3.2	35.4 ± 2.1
L	38.2 ± 2.9	35.1 ± 2.0

In the evaluation of emission quantification after attenuation correction, the results revealing no significant lateral differences between each of the seven regions show that the present implementation was effective without bias towards the left or right side. Although significant differences were found in the quantitative values of the seven regions, the error was less than 40%. The values shown in Table 1 indicate that the degree of underestimation of activity was different for each area. The brain phantom used in this study was designed to simulate the shape of the cerebral cortex, with the thickness of the cortex differing according to the region. For example, the thin portion of the occipital lobe is 3–4 mm thick, whereas the thick portion of the cerebellum is several centimeters. In this study, an ROI with a diameter of 3 mm was placed in the center position of the thickness of the cortex, but we found it difficult to completely avoid partial volume effect in thin regions. As we mentioned in the Scanner Configuration, we confirmed that the contrast for a 10-mm sphere was approximately 50% of the theoretical value because of partial volume effect, and we, therefore, consider that the quantitative differences between regions were within a reasonable error range, and that the attenuation correction method implemented has practical accuracy.

The present study had several limitations. First, we made no comparison with an exact method. In particular, it is necessary to verify the accuracy of our correction in comparison with an attenuation map known to accurately present the attenuation coefficients in the phantom. Second, we could not consider the effect of high-density area that may be present in clinical brain study, such as normal calcification, old infarcted lesion, and post-operative state with metal clipping etc. In particular, it is necessary to evaluate the effect of metals with higher attenuation coefficients than skull, including size dependences. Therefore, we are planning to evaluate these effects as a critical issue in future work. Finally, to obtain an accurate attenuation factor using the ML-ACF algorithm, systematic and statistical errors of randoms, scattering, sensitivity coefficients, and TOF offset must be suppressed as much as possible. In a previous study [2], the accuracy of attenuation factor estimation was evaluated under conditions of accurate scatter estimation.

Table 2 Results of statistical analysis of seven regions using the Tukey–Kramer method

	Frontal lobe	Occipital lobe	Parietal lobe	Temporal lobe	Thalamus	Striatum
Frontal lobe						
Occipital lobe	< 0.01					
Parietal lobe	< 0.01	n.s.				
Temporal lobe	< 0.01	< 0.05	n.s.			
Thalamus	n.s.	< 0.01	< 0.05	n.s.		
Striatum	n.s.	< 0.01	< 0.01	< 0.01	n.s.	
Cerebellum	< 0.05	< 0.01	< 0.01	< 0.01	< 0.01	< 0.01

However, in practice, both the scattering component and the attenuation factor must be estimated from an unknown state, and in the current implementation, the scattered component was calculated using a uniform attenuation map, which may have led to some errors. Although we confirmed the heterogeneity of the head attenuation map, we believe that further optimization will lead to further improvements in accuracy.

Conclusion

The ML-ACF-based attenuation correction implemented for TOF brain PET worked well and demonstrated practical accuracy in the quantification of radioactivity in a cerebral cortex phantom. We expect this individualized approach, which does not require additional transmission scans, to contribute to reducing exposure to ionizing radiation during brain PET scans and to suppressing the position mismatch between the emission and attenuation maps.

Acknowledgements The authors wish to thank Dr. Akira Imoto from the National Cerebral and Cardiovascular Center Hospital, for cooperation with the phantom experiment and useful advice. We also thank the reviewers of this paper for their critical and essential comments to clarify our thesis. We thank Karl Embleton, PhD, from Edanz Group (https://jp.edanz.com/ac) for editing a draft of this manuscript. The part of authors are employees of Shimadzu Corporation. No other potential conflicts of interest relevant to this article exist. Question: can attenuation correction based on ML-ACF provide sufficient attenuation information for brain PET study ? Pertinent findings: in phantom study, the heterogeneous distributions of attenuation coefficients in soft tissue, skull, and nasal cavity were sufficiently visualized. The attenuation-corrected emission values of the cerebral cortex had practical accuracy within the error range. Implications for patient care: the ML-ACF-based attenuation correction implemented in this study may provide a comfortable brain PET scan that can avoid additional radiation exposure and spatial mismatch associated with attenuation correction.

References

1. Defrise M, Rezaei A, Nuyts J. Time-of-flight PET data determine the attenuation sinogram up to a constant. Phys Med Biol. 2012;57:885–99.
2. Rezaei A, Defrise M, Nuyts J. ML-reconstruction for TOF-PET with simultaneous estimation of the Attenuation Factors. IEEE Trans Med Imag. 2014;33(7):1563–72.
3. Frey KA, Lodge MA, Meltzer CC, Peller PJ, Wong TZ, Hess CP, et al. ACR-ASNR practice parameter for brain PET/CT imaging dementia. Clin Nucl Med. 2016;41(2):118–25.
4. Nuyts J, et al. Simultaneous maximum a posteriori reconstruction of attenuation and activity distributions from emission sinograms. IEEE Trans Med Imag. 1999;18(5):393–403.
5. Berkera Y, Li Y. Attenuation correction in emission tomography using the emission data—A review. Med Phys. 2016;43(2):807–32.
6. Kobayashi T, Kitamura K. A solution for scaling problem in joint estimation of activity and attenuation. In: IEEE NSS&MIC Conf. Rec. 2017.
7. Li Y, Matej S, Karp JS. Practical joint reconstruction of activity and attenuation with autonomous scaling for time-of-flight PET. Phys Med Biol. 2020;65:235037.
8. Hudson HM, Larkin RS. Accelerated image reconstruction using ordered subsets of projection data. IEEE Trans Med Imaging. 1994;13(4):601–9.
9. Watson CC, Newport D, Casey ME. A single scatter simulation technique for scatter correction in 3D PET. Three-dimensional image reconstruction in radiology and nuclear medicine. IEEE Trans Med Imaging. 1996;1996:255–68.
10. Nakayama T, Kudo H. Derivation and implementation of ordered-subsets algorithms for list-mode PET data. In: IEEE NSS&MIC Conf. Rec. 2005.
11. Iida H, Hori Y, Ishida K, Imabayashi E, Matsuda H, Takahashi M, et al. Three-dimensional brain phantom containing bone and grey matter structures with a realistic head contour. Ann Nucl Med. 2013;27:25–36.